More Is Better: Acceptor Engineering for Constructing NIR-II AIEgens to Boost Multimodal Phototheranostics

Shiping Yang,[1,5] Jianyu Zhang,[1,5] Zhijun Zhang,[2,]* Weilin Xu,[2] Miaomiao Kang,[2] Xue Li,[2] Dingyuan Yan,[2] Ryan T. K. Kwok,[1] Jianwei Sun,[1] Jacky W. Y. Lam,[1] Dong Wang,[2,]* and Ben Zhong Tang[1,3,4,]*

[1]Department of Chemistry, Hong Kong Branch of Chinese National Engineering Research Center for Tissue Restoration and Reconstruction, State Key Laboratory of Molecular Neuroscience, Division of Life Science, Ming Wai Lau Centre for Reparative Medicine, Karolinska Institutet, and Guangdong-Hong Kong-Macau Joint Laboratory of Optoelectronic and Magnetic Functional Materials, The Hong Kong University of Science and Technology, Kowloon, Hong Kong 999077, China.

[2]Center for AIE Research, College of Materials Science and Engineering, Shenzhen University, Shenzhen 518060, China.

[3]School of Science and Engineering, Shenzhen Institute of Aggregate Science and Technology, The Chinese University of Hong Kong, Shenzhen, Guangdong 518172, China.

[4]Center for Aggregation-Induced Emission, South China University of Technology, Guangzhou 510640, China.

[5]These authors contributed equally: Shiping Yang, Jianyu Zhang.

*Corresponding emails: tangbenz@cuhk.edu.cn (Ben Zhong Tang); wangd@szu.edu.cn (Dong Wang); zhijunzhang@szu.edu.cn (Zhijun Zhang)

Abstract: The manipulation of electron donor/acceptor (D/A) shows endless impetus for innovating optoelectronic materials. Because of the diversity of electron-donating species, the study on donor engineering has explored systematically, whereas the research on electron acceptor engineering received a snub by contrast. Inspired by the philosophical idea of "more is different", two systems with D′−D−A−D−D′ (1A system) and D′−D−A−A−D−D′ (2A system) structures based on the acceptor engineering were ingeniously designed and studied. It was demonstrated that the 1A system presented a weak aggregation-induced emission (AIE) to aggregation-caused quenching (ACQ) phenomenon along with the increased acceptor electrophilicity. Interestingly, the 2A system exhibited an opposite ACQ-to-AIE transformation, manifesting the dual-acceptor tactic could facilitate AIE activity. Owing to the highest molar absorptivity, second near-infrared emission, superior AIE property, favorable production ability of reactive oxygen species and excellent photothermal conversion efficiency, a representative member of 2A system handily performed in multimodal imaging-guided photodynamic-photothermal synergetic therapy for efficient tumor elimination.

Introduction

Nature is a complex and multifaceted system, and each constituent performs its own function. That is to say, when many individual components are assembled or admixed into a collective group/aggregate, there could produce superior outputs and simultaneously execute multiple tasks (beyond independent components)[1,2]. Aristotle, a Greek philosopher in the Classical period, has already pioneered the emergentism view that "The whole is greater than the sum of its parts". This heuristic epistemology is consistent with the philosophical perspectives of "quantity breeds quality" and "more is different"[3]. Unambiguously, the field of materials science has achieved flourishing developments under the guidance of such research philosophies, especially for luminescent materials[4–6].

Promoting the advancement of luminescent materials would undoubtedly facilitate the high-tech innovation and benefit societal progress[7–10]. There are mainly two general tactics for manipulating the luminescence color, absorption/emission wavelength, molar absorptivity (ε), and luminescence efficiency of luminescent materials[11]. One feasible way is to subtly regulate the conjugation extent of a molecular skeleton. However, it should be pointed out that the red-shift in the absorption/emission wavelength caused by extending the π-conjugation could lead to the risk of strengthening the detrimental π–π stacking interaction[5,12,13]. Alternatively, electron donor–acceptor (D–A) engineering provides a sophisticated and profound combination protocol[9,14–16]. Due to the variety (e.g., carbazole, diphenylamine, triphenylamine) and accessible modification of electron donors, feasibly customized optical properties, and promising functionalities, the construction of organic small-molecule fluorophores with D–A–D-type scaffolds have attracted immense attention[11,17,18]. As a rule, the highest occupied molecular orbital (HOMO) is broadly delocalized along the whole conjugated molecular backbone, but the lowest unoccupied molecular orbital (LUMO) is almost distributed on the acceptor moiety in those fluorophores. Thus, the manipulation of electron acceptor could exert a greater impact on the structure-property relationships of D–A–D fluorophores. Unfortunately, although enthusiastic research endeavors have been injected in the past few decades, especially in organic photovoltaic field[19–22], the number of practical electron acceptors with distinct electron-withdrawing ability for pursuing tunable and high-performance fluorophores are still limited. Inevitably, employing the acceptor engineering to develop novel and multifunctional fluorophores remain as a bottleneck and receive a stagnancy up to now[23,24]. In this circumstance, how to make full use of the existing and typical electron acceptors to excavate the undisclosed realm of multi-acceptors ("more") in a D–A–D skeleton, is anticipated to be an exotic and exciting wonderland with limitless treasures, which could breed a conspicuous molecular design philosophy.

On the other hand, fluorophores are practically frequently used as a whole in the aggregate state, rather than in their single-molecule state, such as in the areas of optoelectronic devices and bioimaging[7,10]. However, traditional luminescent molecules generally suffer from the problem of aggregation-caused quenching (ACQ), which gives rise to the result that a separated

element is more brilliant than the whole, meaning more is worse[12,13,25]. Fortunately, this common belief of ACQ is subverted by the phenomenon of aggregation-induced emission (AIE), which is exactly opposite to the ACQ effect and the collaboration and synergism from many isolated molecules in the aggregate state ("more") promote it to perform better than its elementary compositions[26,27]. For AIE phenomenon, non-emissive luminogens in the monodispersed state are induced to emit intensely upon the formation of aggregates, which could be understood by the mechanism of restriction of intramolecular motions (RIM)[5]. Furthermore, aggregation generally induces the divergence (the multipath distribution of excitons), in which the equilibrium between radiative and nonradiative decays could be subtly regulated to generate a multifunctional system[28]. The distinct behaviors and qualitative jumps after forming aggregates from a simple molecule could be ascribed to the change of morphologies, quantities, or diverse interactions that render manifold properties in the aggregate state[27]. Overall, AIE effect is a representative example exhibiting a non-linear addition of properties from simple molecules to versatile aggregates[29,30]. In this regard, the AIE technology offers a new platform and territory for researchers to explore and access the philosophy of "more is better".

As a proof-of-concept, in this work, acceptor engineering was systematically studied by using two approaches. Firstly, as shown in Fig. 1a, four small molecules with a structural type of D′−D−A−D−D′ were designed and classified as 1A system. These four molecules possess the same electron donor but different electron acceptors with an orderly increased electrophilic capability from benzo[2,1,3]thiadiazole to ben-zo[1,2-c:4,5-c′]bis([1,2,5]thiadiazole). Furthermore, to explore the property changes that resulted from introducing one more acceptor at the molecular level, the construction of 2A system with the molecular structure of D′−D−A−A−D−D′ was conducted. More importantly, the essence or disparity of the optical behaviors of these two systems entices us to unravel the veil in their aggregate states. The results revealed that the 1A system encountered a change of photophysical properties from weak AIE to ACQ upon enhancing the electron-withdrawing capacity of the acceptors. In contrast, the 2A system demonstrated an opposite ACQ-to-AIE transformation (Fig. 1a). Strikingly, the members of 2A system possessed a higher ε than their counterparts in the 1A system, no matter which acceptor was utilized. In addition, among all the molecules of 2A system, 2TT-2BBTD with the strongest electron acceptor exhibited the highest ε, best AIE activity, and longest fluorescence emission wavelength located in the second near-infrared (NIR-II, 1000–1700 nm) region. These advantageous properties, together with appreciable reactive oxygen species (ROS) and prominent photothermal generation, jointly enabled 2TT-2BBTD nanoparticles (NPs) to serve as an ideal NIR-II fluorescence imaging (FLI)-featured multimodal phototheranostic system for breast cancer elimination in live mice (Fig. 1b, c). This work definitely exemplifies the molecular design philosophy of "more is better" and provides a new avenue for developing multifunctional phototheranostic systems.
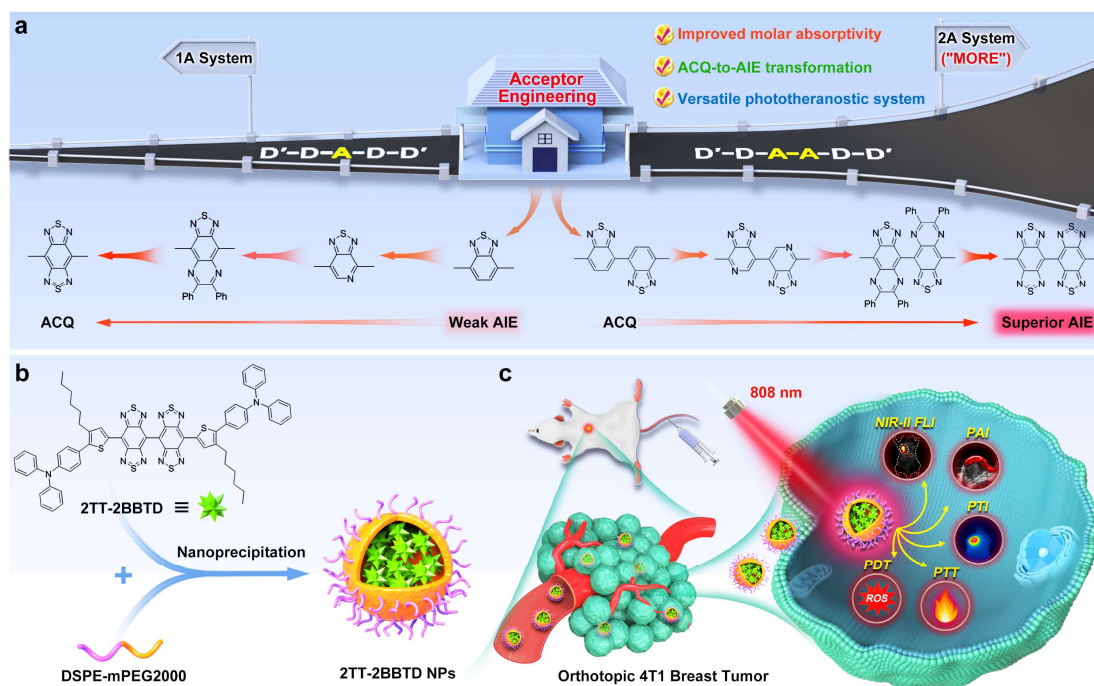
Fig. 1 Schematic illustration of the investigation on acceptor engineering, nanofabrication and multifunctional phototheranostic application. a Molecule types and the structures of diverse acceptors employed in the 1A or 2A system. **b** Molecular structure of 2TT-2BBTD and the preparation of 2TT-2BBTD NPs by a nanoprecipitation method. **c** Application of 2TT-2BBTD NPs in NIR-II fluorescence-photoacoustic-photothermal trimodal imaging-guided photodynamic-photothermal synergetic therapy of cancer.

Results

Design, synthesis and characterization. To systematically study the effect of acceptor engineering in modulating the photophysical properties of luminogens at the molecular and aggregate levels, four frequently used electron acceptors were employed to construct luminogens with one or two acceptor units, respectively (Fig. 2a, e). To be specific, in the 1A system, benzo[2,1,3]thiadiazole (BTD), pyridal[2,1,3]thiadiazole (PTD), 6,7-diphenyl-[1,2,5]thiadiazolo[3,4-*g*]quinoxaline (DPTDQ) and benzo[1,2-c:4,5-c′]bis([1,2,5]thiadiazole) (BBTD) with the progressively increased electron-withdrawing ability were selected as the electron acceptors. Besides, alkyl thiophene serving as both π-conjugation bridge and electron donor, and triphenylamine (TPA) unit acting as the second donor and molecular rotor were integrated to produce D′−D−A−D−D′-type molecules. The long alkyl chains were introduced as shielding units to provide steric hindrance, which could weaken the intermolecular interactions and facilitate the intramolecular motions even within NPs[31]. Particularly, the alkyl group on the thiophene ring close to the TPA unit could enable a longer absorption wavelength[32]. In addition, the molecules in the 2A system with D′−D−A−A−D−D′ structure were established through grafting one more electron acceptor in comparison with their counterparts in the 1A system. The synthetic routes of molecules in the 1A (including 2TT-BTD, 2TT-PTD, 2TT-

DPTDQ and 2TT-BBTD) and 2A (including 2TT-2BTD, 2TT-2PTD, 2TT-2DPTDQ and 2TT-2BBTD) systems were provided in the Supplementary Information (Supplementary Figs. 1−6), and their structures were satisfactorily characterized by NMR and mass spectroscopy (Supplementary Figs. 7−65).
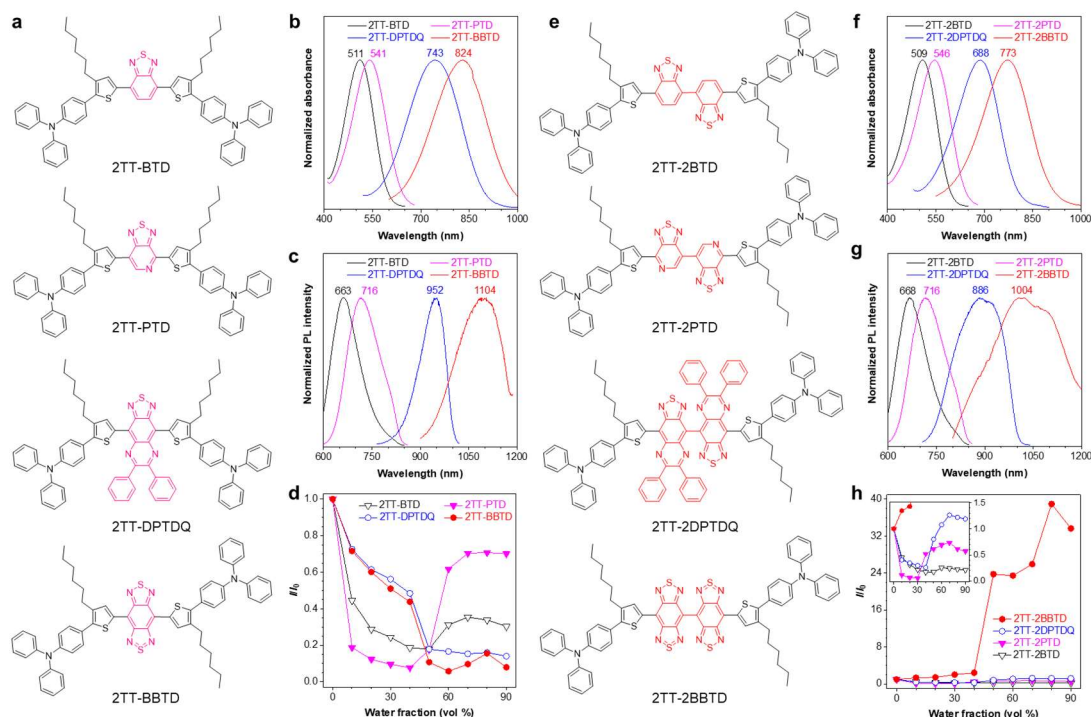

Fig. 2 The designed compounds and photophysical properties. a, **e** Chemical structures of 2TT-BTD, 2TT-PTD, 2TT-DPTDQ, 2TT-BBTD, 2TT-2BTD, 2TT-2PTD, 2TT-2DPTDQ and 2TT-2BBTD, respectively. **b**, **f** Normalized absorption spectra in THF solution. **c**, **g** Normalized emission spectra in THF solution. **d**, **h** Plots of the relative emission intensity (I/I_0) versus the composition of the THF/H$_2$O mixture, where I_0 = PL intensity in pure THF solution. Inset: partially enlarged I/I_0 plots of 2TT-2BTD, 2TT-2PTD, 2TT-2DPTDQ and 2TT-2BBTD, respectively. Concentration = 10 μM.

Subsequently, the photophysical properties of the molecules in the 1A system were investigated by measuring their UV-Vis-NIR absorption and photoluminescence (PL) spectra. It was noticeable that the absorption and emission maxima of these four luminogens showed obvious red shifts in THF solution by orderly changing the electron acceptor unit from BTD to BBTD (Fig. 2b, c). 2TT-BBTD exhibited the strongest intramolecular charge transfer (ICT) effect than the other three compounds, which could be reflected by their low-energy charge transfer (CT) absorption bands that steadily increased in the sequence of 511, 541, 743, and 824 nm for 2TT-BTD, 2TT-PTD, 2TT-DPTDQ and 2TT-BBTD, respectively (Fig. 2b). Additionally, their corresponding emission maxima were also gradually bathochromic shift in the line of 663, 716, 952 and 1104 nm, demonstrating that the enhanced ICT effect was derived from the elaborate acceptor engineering.

The PL intensity fluctuations of these four molecules in THF/H$_2$O mixtures with different water fractions (f_w) as poor solvent were further evaluated. As illustrated in Fig. 2d and Supplementary Fig. 66, for 2TT-BTD and 2TT-PTD, upon gradually increasing the f_w to 40%, their emission intensities decreased significantly due to the twisted intramolecular charge transfer (TICT) effect[33,34], which then turned to slightly enhance along with further elevating the f_w. As a whole, 2TT-BTD and 2TT-PTD analogously displayed the features of TICT plus weak AIE. However, 2TT-DPTDQ and 2TT-BBTD exhibited a typical ACQ phenomenon with the characteristics of obviously decreased fluorescence intensities as aggregates in comparison to the isolated molecules. Definitely, at f_w = 90%, the I/I_0 values (I_0 is the PL intensity of molecules in pure THF solution) of 2TT-DPTDQ and 2TT-BBTD were determined to be as low as 0.14 and 0.08, respectively. In addition, the solvatochromic effects of the molecules in the 1A system were carried out to verify the TICT property. With the increase of solvent polarity, the red-shifted emission maxima and weakened PL intensities were monitored along with the negligible variations in the corresponding absorption spectra (Supplementary Fig. 67). These results fully signified the TICT behavior of these four luminogens. As a whole, the D′−D−A−D−D′-type molecules in the 1A system exhibited the conversion of AIE activity to ACQ behavior in the wake of employing acceptor with enhanced electron deficiency.

To probe the photophysical properties of the 2A system, their absorption and emission spectra in THF solution were measured. At the molecular level, these four compounds affirmed the concrete bathochromic shifts both in absorption maxima (509, 546, 688, and 773 nm) and emission maxima (668, 716, 886, and 1004 nm) from 2TT-2BTD to 2TT-2BBTD (Fig. 2f, g), respectively, attributed to the orderly enhanced electron-withdrawing ability of the electron acceptors. Compared with the 1A system, interestingly, the corresponding luminogens with one more acceptor in the 2A system possessed a definitely higher ε, which furnished an attractive and robust strategy to improve the molecular light-harvesting ability (Supplementary Fig. 68). It is worth noting that 2TT-2BBTD was resplendently standing out from the others owing to its highest ε (4.29 × 10^4 M^{-1} cm^{-1}) and maximum emission peak in the NIR-II region, which laid a solid foundation for the multimodal phototheranostics application (Supplementary Fig. 68d)[35,36]. Moreover, since an 808 nm laser is frequently used in phototheranostics due to its minimal biological absorption and superior penetration depth in biological tissue, the ε of a phototheranostic agent at 808 nm will definitely determine the phototheranostic outcome. Gladly, the ε of 2TT-2BBTD at 808 nm was still as high as 3.76 × 10^4 M^{-1} cm^{-1}, which was higher than that of a majority of previously developed NIR-II AIE luminogens (AIEgens)[16,37,38]. Therewith, the PL of molecules in the 2A system was studied in THF/H$_2$O mixtures with different f_w. As displayed in Fig. 2h and Supplementary Fig. 69a, the PL intensities of 2TT-2BTD decreased prominently from the molecularly dispersed state in THF solution (f_w = 0) to the aggregate state, where an ACQ appearance was monitored. In contrast, benefitting from the elaborate acceptor engineering, 2TT-2PTD, 2TT-2DPTDQ and 2TT-2BBTD revealed the sequential promotion of the AIE effect, as evidenced by their gradually increased I/I_0 values of

0.57, 1.19 and 33.65 at f_w = 90%, respectively (Fig. 2h and Supplementary Fig. 69b−d). Meanwhile, the intrinsic TICT characteristic of compounds in the 2A system was also proved by their AIE curves and solvatochromic effects (Fig. 2h and Supplementary Fig. 70). To sum up, by virtue of the acceptor engineering strategy, the compounds in the 2A system with the molecular structure of D′−D−A−A−D−D′ demonstrated the transformation of ACQ-to-AIE, which nourished the magnificent AIE property of 2TT-2BBTD ultimately.

Theoretical calculation. To obtain more in-depth insights into the opposite photophysical properties of the 1A and 2A systems, the geometries of all molecules were optimized using the density functional theory (DFT) method. As illustrated in Fig. 3a−h, the compounds in 1A and 2A systems showed the dihedral angles of 40−48° between the twisted TPA and alkyl thiophene units. Clearly, the 1A system demonstrated gradually decreased dihedral angles of the thiophene-acceptor-thiophene core (from 6.7° in 2TT-BTD to 1.1° in 2TT-BBTD), which stemmed from the orderly attenuated repulsion effect between the hexyl chain in the thiophene ring and the adjacent acceptor unit. In this context, together with the enhanced D−A and TICT effects, the more coplanar backbone would strengthen the intermolecular interactions and nonradiative decay to produce the ACQ effect[32,34]. In the case of 2A system, interestingly, the elevated dihedral angles of two acceptors (from 32° in 2TT-2BTD to 55° in 2TT-2BBTD) were triggered by well-designed acceptor engineering. Thus, it would be reasonable that the distorted backbone of the thiophene-acceptor-acceptor-thiophene moiety played a key role in realizing the transformation of ACQ to AIE in the 2A system. The ACQ effect could be suppressed effectively by employing more electrophilic and twisted dual-acceptor. Particularly, a more twisted conformation could provide a more flexible environment and higher degree of freedom for intramolecular motions, thus leading to an extremely low PL intensity (I_0) of 2TT-2BBTD in the solution state. Upon the aggregate formation, the intramolecular motions of 2TT-2BBTD were restricted to some extent, and gradually enhanced emission intensities were monitored due to the RIM mechanism, to give rise to the increased I/I_0 values. Taken together, the prominent AIE activity of 2TT-2BBTD prevailed over the dark TICT effect plus the weak intermolecular interactions in the aggregate state.
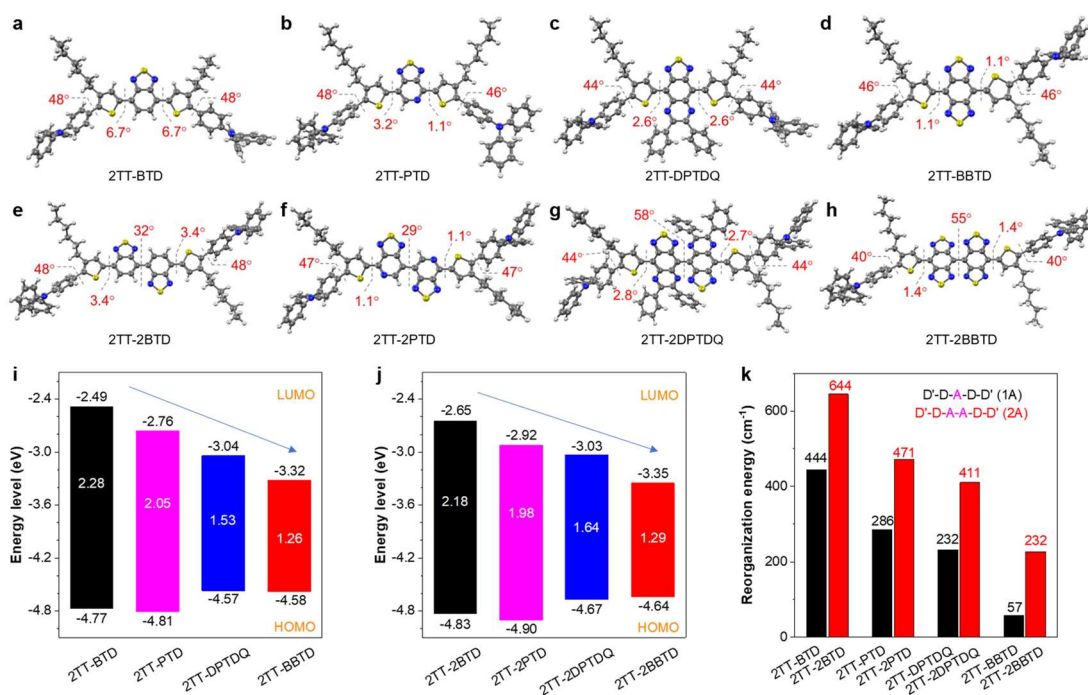
Fig. 3 Theoretical calculation analysis. a–h Optimized ground-state geometries of all compounds in the 1A and 2A systems. **i, j** Calculated energy levels of all compounds in the (i) 1A system and (j) 2A system. **k** Plots of the reorganization energy contributed by the dihedral angle change between the ground-state and excited-state geometries.

Then, the frontier molecular orbitals of all compounds were calculated based on the optimized ground-state geometries. As demonstrated in Supplementary Fig. 71, the HOMO orbitals delocalized across the whole molecular skeleton, while the LUMO was mainly distributed on the central core of the acceptor and thiophene units. The energy gaps between HOMO and LUMO were determined to be 2.28, 2.05, 1.53, and 1.26 eV for compounds in the 1A system, respectively (Fig. 3i). Similarly, a decreased trend of 2.18, 1.98, 1.64, and 1.29 eV was observed for compounds in the 2A system (Fig. 3j). These orderly narrow energy gaps were consistent with the red-shifted absorption and emission wavelengths of the compounds in 1A and 2A systems along with the increased electron-withdrawing ability of acceptors. Notably, the energy levels of LUMO in the 1A or 2A system exhibited an obviously downward trajectory along with the slightly upraised energy levels of HOMO. This confirmed that the untraversed acceptor engineering could be a credible tactic to construct luminescent materials with desirable absorption and emission wavelengths. In addition, the reorganization energies (λ) of these compounds were calculated, which could quantitatively describe the inherent geometry changes and intramolecular motions upon photoexcitation[39]. Moreover, the contribution from the dihedral angle (at low-frequency region with wavenumbers < 500 cm^{-1}) to the total λ was prone to reflect the intramolecular twisting motions to nonradiative decay[40]. Interestingly, the introduction of one more acceptor in the 2A system endowed a higher contribution of dihedral angle to the total λ than that of the counterparts in the 1A system (Fig. 3k and Supplementary

Fig. 72). These outcomes indicated that the compounds in 2A system exhibited a higher proportion of nonradiative decay and potential for photothermal conversion than those in the 1A system.

Preparation and characterization of nanoparticles. Considering the eminent AIE feature and emission wavelength located in the NIR-II region, the hydrophobic 2TT-2BBTD was encapsulated into NPs using an amphiphilic co-polymer called DSPE-mPEG2000 (Fig. 1b). Hence, the prepared NPs were endowed with improved biocompatibility and water dispersity. Dynamic light scattering (DLS) analysis revealed that the average hydrodynamic diameter of 2TT-2BBTD NPs was about 66.76 nm with a desired polydispersity index of 0.165 (Fig. 4a). Furthermore, transmission electron microscope (TEM) measurement clarified that these NPs hold a spherically shaped morphology with a particle size of approximately 40 nm. Noteworthy, 2TT-2BBTD NPs displayed excellent storage stability both in deionized water and PBS buffer under ambient condition for at least four weeks (Supplementary Fig. 73a). The particle size of 2TT-2BBTD NPs also maintained a good colloidal stability in PBS + FBS (10%) solution over 4 days (Supplementary Fig. 73b). In view of the fact that 2TT-DPTDQ, 2TT-2DPTDQ and 2TT-BBTD also hold the potential for intravital applications due to their NIR emission, their corresponding NPs were prepared via the same nanoprecipitation method with average sizes of 64.17, 72.38 and 119.20 nm, respectively (Supplementary Fig. 74). To investigate their ability for NIR FLI, the relative quantum yields (QYs) of 2TT-DPTDQ, 2TT-2DPTDQ, 2TT-BBTD and 2TT-2BBTD in both single-molecule state (THF solution) and NPs state were determined. By using indocyanine green (ICG) as a reference, the QYs of 2TT-DPTDQ and 2TT-DPTDQ NPs were determined to be 1.18% and 0.31%, respectively (Supplementary Fig. 75a–i). The QY of 2TT-2DPTDQ NPs (1.59%) was slightly higher than that of 2TT-2DPTDQ (1.23 %) in THF solution (Supplementary Fig. 75j–o). Meanwhile, the QYs of 2TT-BBTD, 2TT-2BBTD and their corresponding NPs in the NIR-II region were also measured by adopting IR-26 as a reference (Supplementary Fig. 76). Obviously, the QY of 2TT-BBTD (3.14%) in THF solution sharply declined to 0.19% in NPs. As expected, the QY of 2TT-2BBTD NPs enhanced by more than thrice to 0.25%, compared with the QY (0.08%) in the solution state. These results again suggested the inherent AIE nature of 2TT-2DPTDQ and 2TT-2BBTD, but both 2TT-DPTDQ and 2TT-BBTD clearly showcased the ACQ characteristics, respectively.
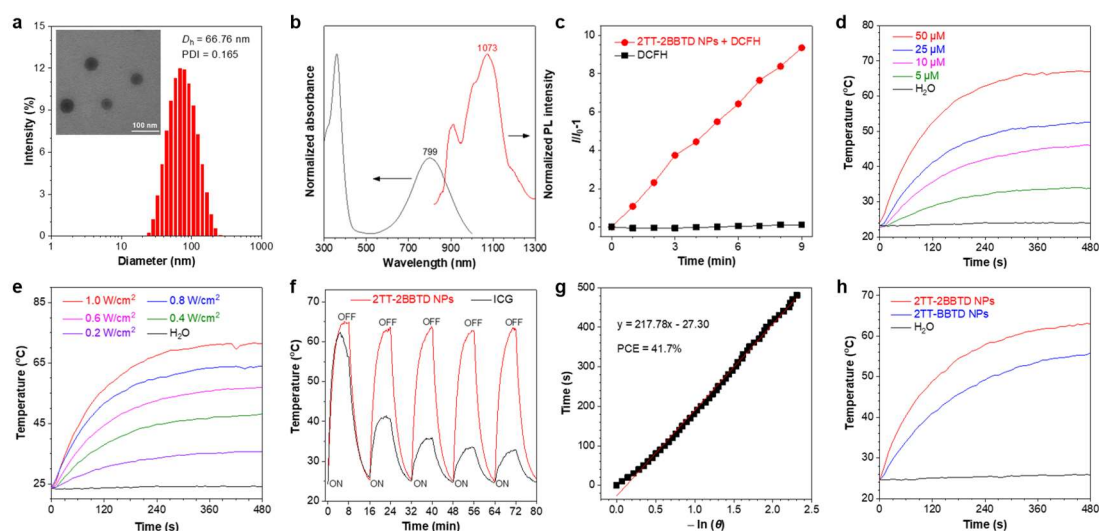
Fig. 4 Characterization of 2TT-2BBTD NPs. a DLS analysis of 2TT-2BBTD NPs. Inset: TEM image of 2TT-2BBTD NPs. **b** The absorption and emission spectra of 2TT-2BBTD NPs in aqueous solution. **c** ROS generation of 2TT-2BBTD NPs (10 μM 2TT-2BBTD) upon 808 nm laser irradiation. **d, e** Temperature elevation of 2TT-2BBTD NPs in aqueous solution with different concentrations and at different power densities under 808 nm laser irradiation, respectively. **f** Photothermal stability of 2TT-2BBTD NPs (50 μM 2TT-2BBTD) and ICG (50 μM) in aqueous solution during five heating-cooling cycles under 808 nm laser irradiation (0.8 W/cm^2). **g** The linear fitting of time from the cooling period versus the negative natural logarithm of driving force temperature for 2TT-2BBTD NPs. **h** Temperature profile of 2TT-BBTD NPs (50 μM 2TT-BBTD), 2TT-2BBTD NPs (50 μM 2TT-2BBTD) and pure water irradiated by 808 nm laser (0.8 W/cm^2) for 8 min.

Due to the excellent properties, 2TT-2BBTD NPs were selected for further photophysical study and bioapplications. The UV-Vis-NIR absorption and PL spectra disclosed that 2TT-2BBTD NPs showed absorption and emission maxima at 799 and 1073 nm, respectively (Fig. 4b). Notably, the spectral tail of 2TT-2BBTD NPs was observed to extend to 1300 nm, providing a superiority for in vivo applications due to the deep tissue penetration of NIR-II emission. Furthermore, the ROS generation and photothermal conversion capacities of 2TT-2BBTD NPs were evaluated. As illustrated in Fig. 4c and Supplementary Fig. 77, along with the continuous laser irradiation, the PL signal of dichlorofluorescein (DCFH) at 525 nm was strengthened rapidly in the presence of 2TT-2BBTD NPs, while negligible elevation in fluorescence intensity was monitored for the solution of DCFH alone. This nearly 10-fold higher fluorescence intensity of DCFH than the initial value after 9 min laser exposure manifested the favorable ROS generation ability of 2TT-2BBTD NPs. Additionally, it was also proved that 2TT-2BBTD NPs possessed the characteristics of NPs concentration- and laser power density-dependent temperature elevation (Fig. 4d, e). These results suggested that the heat generation from 2TT-2BBTD NPs can be facilely manipulated. Noticeably, the temperature of 2TT-2BBTD NPs in aqueous solution reached to the plateau at 66 °C at a low

concentration of 50 μM under 808 nm laser irradiation (0.8 W/cm^2) for 8 min, demonstrating the considerable photothermal conversation performance. After five consecutive cycles of the heating-cooling process, 2TT-2BBTD NPs also retained splendid and unaltered photothermal generation ability (Fig. 4f). In sharp contrast, the photothermal stability of ICG showed a poor performance and decreased by nearly 50% under the same conditions. Thereupon, the photothermal conversion efficiency (PCE) of 2TT-2BBTD NPs was determined to be 41.7% (Fig. 4g). As expected, 2TT-2BBTD NPs revealed superior heat generation ability to 2TT-BBTD NPs under the same circumstances (Fig. 4h and Supplementary Fig. 78). It could be ascribed to the introduction of one more acceptor into the 1A system, which could result in intensive intramolecular twisting motions on account of the increased contribution of dihedral angle change to the total λ (Fig. 3k).

In vitro experiments. Encouraged by the great potential of 2TT-2BBTD NPs in multimodal phototheranostics, the synergistic phototherapeutic efficacy was firstly assessed at the cellular level. For easy observation, the fluorescein isothiocyanate (FITC)-labeled 2TT-2BBTD NPs, abbreviated as FITC-2TT-2BBTD NPs were prepared. Imaging using confocal laser scanning microscopy (CLSM) was then carried out to investigate the intracellular uptake behavior. As shown in Fig. 5a, an obvious co-localization of fluorescence signal between FITC-2TT-2BBTD NPs and LysoTracker Red was monitored, suggesting that 2TT-2BBTD NPs entered the 4T1 cells possibly through a lysosome-mediated endocytosis pathway. Next, CCK-8 assay was performed to evaluate the tumoricidal effect of 2TT-2BBTD NPs in vitro (Fig. 5b). Obviously, negligible toxicity to 4T1 cancer cells was detected even at a high concentration of 2TT-2BBTD NPs under dark condition, revealing its desired biocompatibility. After NIR laser irradiation at 808 nm and 0.6 W/cm^2, more than 70% cell viability was still detected at a dye concentration was lower than 10 μM, while almost all the 4T1 cells were deactivated by increasing the dye concentration to 50 μM. Besides, the half-maximal inhibitory concentration (IC$_{50}$) of 2TT-2BBTD NPs to 4T1 cells was determined to be 13.6 μM based on 2TT-2BBTD, demonstrating its excellent cytocidal activity upon laser irradiation. The phototherapeutic effect of 2TT-2BBTD NPs was further verified by the co-stained approach using fluorescein diacetate (FDA) and propidium iodide (PI), where the green and red fluorescence were responsible for live and dead cells, respectively. The staining results displayed that a strong green fluorescence signal was obtained in the groups of PBS, PBS + laser (L), and 2TT-2BBTD NPs (dark condition), whereas nearly all of the 2TT-2BBTD NPs-loaded 4T1 cells entered the death state upon laser irradiation (Fig. 5c). Furthermore, flow cytometric analysis was also conducted by employing Annexin V-FITC detection assay to elucidate the cell death mechanism of cells. As illustrated in Fig. 5d, 56.0% of 4T1 cells were involved in the apoptosis pathway after treatment with 2TT-2BBTD NPs plus laser irradiation (2TT-2BBTD NPs + L), and 20.4% of cancer cells were related to necrosis. However, the unobtrusive apoptosis or necrosis was surveyed in other control groups. Taken together, the inappreciable side effect of the operational laser power

density (808 nm, 0.6 W/cm^2), outstanding biocompatibility, and photoinduced cytocidal ability of 2TT-2BBTD NPs are incontrovertible.
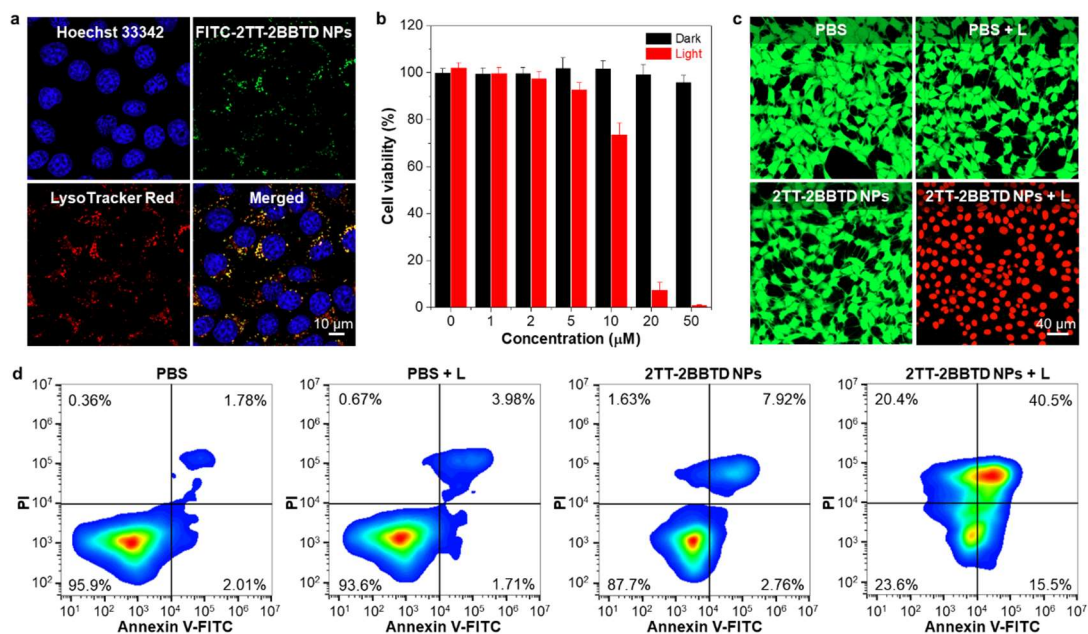

Fig. 5 In vitro phototherapy application. a CLSM images of 4T1 cells after being stained with Hoechst 33342, FITC-2TT-2BBTD NPs, and LysoTracker Red. **b** Cell viability of 4T1 cells after being treated with different concentrations of 2TT-2BBTD NPs under dark or 808 nm laser irradiation (0.6 W/cm^2). **c** Live/dead cell staining of 4T1 cells after various treatments. The green and red fluorescence mean live and dead cells, respectively. **d** Flow cytometric analysis of 4T1 cells treated with PBS and 2TT-2BBTD NPs (50 μM 2TT-2BBTD) with or without laser irradiation (808 nm, 0.6 W/cm^2).

In vivo phototheranostics. Inspired by the glorious NIR-II fluorescence and in vitro cytocidal efficacy, the multimodal imaging-guided phototherapy performance of 2TT-2BBTD NPs was investigated based on an orthotopic 4T1 breast tumor mouse model. Preliminarily, the NIR-II FLI and accumulation ability of 2TT-2BBTDNPs in the tumor site were estimated. Before injection of 2TT-2BBTD NPs, the mice exhibited extremely feeble autofluorescence interference upon using the long-pass filter of 1000 nm, which could provide a minimal background signal. After intravenous injection of 2TT-2BBTD NPs, the fluorescence signal gradually arose and increased in the tumor region over time, suggesting a desirable tumor-site accumulation ability (Fig. 6a). Particularly, a fluorescence intensity reached its maximum at 12 h post-injection and subsequently became weaker due to the metabolism (Fig. 6a and Supplementary Fig. 79a). In order to quantitatively analyze the bio-distribution of 2TT-2BBTD NPs after 24 h injection, the tumor tissue and major organs were isolated. As illustrated in Supplementary Fig. 79b–c, it was affirmed that a distinct fluorescent signal was found in the tumor region, while the fluorescent emission in liver and spleen was also visualized. Consistent with the results of FLI, the photoacoustic signal also presented a maximum level at 12 h and

maintained for 24 h after tail vein injection (Fig. 6b and Supplementary Fig. 80). There is no doubt that the synergism of FLI and photoacoustic imaging (PAI) would be a powerful weapon to visualize and diagnose tumor. Considering that 2TT-2BBTD NPs possessed a substantial heat generation capacity, in vivo photothermal imaging (PTI) was conducted by using 808 nm laser (0.6 W/cm^2) as an illumination source after 12 h intravenous administration of the NPs. According to the infrared thermal images shown in Fig. 6c, a rapid temperature increment from 32.8 to 62.3 °C in the tumor site only within 2 min irradiation was recorded, and a temperature plateau of about 65.5 °C was observed after 4 min irradiation. In contrast, the saline-treated mouse indicated negligible temperature elevation under the same circumstance, again demonstrating the reliable photothermal conversion performance of 2TT-2BBTD NPs (Supplementary Fig. 81). Collectively, these results strongly manifested that 2TT-2BBTD NPs possessing NIR-II FLI, PAI, and PTI functions would be an impressive diagnostic agent for precise cancer therapy.

Later on, the in vivo antitumor efficacy of 2TT-2BBTD NPs was assessed by randomly dividing the orthotopic 4T1 breast tumor (~100 mm^3)-bearing mice into four groups. Upon merely a single intravenous injection of the NPs for 12 h and followed once laser exposure (808 nm, 0.6 W/cm^2, 10 min), the growth of the solid neoplasms was thoroughly suppressed and almost eliminated at day 3 in the phototherapeutic group of 2TT-2BBTD NPs plus laser irradiation (Fig. 6d). After 15-day treatment, full tumor eradication and undetected recurrence were realized, where the treated mice were only left behind with a scar (Fig. 6d and Supplementary Fig. 82). The tumor volumes in other three groups (saline, saline plus laser irradiation, and 2TT-2BBTD NPs alone) grew rapidly and delivered no inhibition effect on the tumor growth (Fig. 6d). On the other side, the histological and immunohistochemical analyses of the tumor slices were also adopted to verify the in vivo therapeutic mechanism of 2TT-2BBTD NPs. As depicted in Fig. 6e, the hematoxylin and eosin (H&E) assay exhibited that extensive destruction of tumor tissues was confirmed in the therapeutic group of 2TT-2BBTD NPs plus laser irradiation. In contrast, the tumor cells still remained a vibrant and dense arrangement in the control groups. The denouement of severe apoptosis or necrosis of the treated 4T1 cells (underwent PDT plus PTT) was proved by the TUNEL staining. Meanwhile, after being treated with 2TT-2BBTD NPs plus laser exposure, the inhibited vessel formation and suppressed cell proliferation of the tumor region were further convinced according to the CD31 and Ki67 staining (Fig. 6e). These outcomes solidly manifested that the synergistic PDT and PTT could afford the exciting therapeutic efficiency of 2TT-2BBTD NPs in vivo.
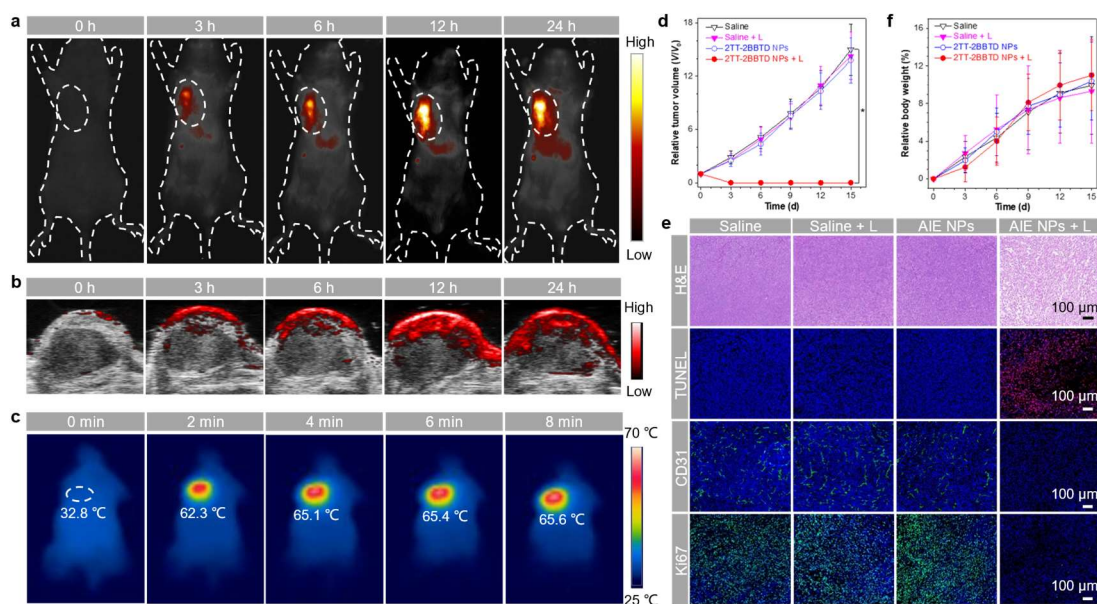
Fig. 6 The investigation of in vivo multimodal phototheranostics and therapeutic mechanism. a NIR-II fluorescence and **b** photoacoustic imaging of orthotopic 4T1 breast tumor-bearing BALB/c mice at different time after intravenous injection of 2TT-2BBTD NPs (λ_{ex} = 808 nm, 2 mM 2TT-2BBTD, 200 μL), respectively. **c** Photothermal imaging of 4T1 tumor-bearing mice treated with 2TT-2BBTD NPs through intravenous injection, followed (12 h later) by 808 nm laser irradiation (0.6 W/cm^2) for 2, 4, 6, and 8 min, respectively. **d** Time-dependent tumor growth curves of 4T1 tumor-bearing mice (n = 5) after various treatments, respectively. **e** H&E, TUNEL, CD31, and Ki67 staining analyses of tumor tissues under various treatments. AIE NPs = 2TT-2BBTD NPs. **f** Body weight changes of 4T1 tumor-bearing mice (n = 5) during the treatments.

In addition, in vivo biosafety of 2TT-2BBTD NPs was also systematically evaluated. During the whole therapeutic course, negligible mouse body weight losses were observed along with similar growth tendencies in these four groups (Fig. 6f). After accomplishing the various treatments at day 15, the mice were sacrificed and analyzed. Results from H&E staining of major organs revealed that the heart, liver, spleen, lung, and kidney had no pathological anomalies or inflammatory lesions (Supplementary Fig. 83). In contrast to the seriously abnormal routine blood indexes in the other control groups, all the measured parameters of the mice in the group of 2TT-2BBTD NPs plus laser irradiation belonged to normal ranges (Supplementary Table 1). Moreover, the blood biochemistry test of hepatic and renal function indicators displayed the comparable results in these four groups, respectively, and no significant statistical difference was observed (Supplementary Fig. 84). Overall, the above-mentioned results exemplified that the acceptor engineering and "more" strategy could provide the versatile phototheranostics system for cancer elimination accompanying with desirable biocompatibility and biosecurity.

Discussion

In this work, we tactfully designed and synthesized four pairs of luminogens with one electron acceptor (1A system) and dual-connected electron acceptors (2A system) based on the strategy of acceptor engineering. Among them, the red-shifted absorption and emission wavelengths were accomplished through modulating the acceptor with incremental electron-withdrawing capability. Because of the gradually enhanced TICT effect and planar π-conjugated structure, the features of these compounds in 1A system showed a change from AIE to ACQ. Excitingly, the 2A system exhibited the transformation of ACQ to AIE behavior, where more distorted molecular conformation (especially for the twist between two acceptor units) and RIM mechanism played critical roles. This clear distinction suggested the effectiveness of the acceptor engineering and "more" strategy in guaranteeing AIE property. Eminently, among all the compounds, 2TT-2BBTD exhibited the most splendid AIE feature, the highest ε, and the satisfactory NIR-II emission. In addition, 2TT-2BBTD NPs were proven to show favorable ROS generation and appreciable photothermal conversion capacities. Accordingly, the trimodal NIR-II FLI/PAI/PTI-guided PDT and PTT for eradicating the orthotopic 4T1 mouse breast tumor was successfully realized by employing 2TT-2BBTD NPs as a phototheranostic agent. Beyond all doubt, this strategy not only offers a spiffy and robust route to improve ε, AIE activity, and photo-driven heat generation ability, but also highlights the success of the proposed molecular design concept of "more is better". By employing this distinctive paradigm of acceptor engineering, it is anticipated that a series of high-performance and novel all-round phototheranostic agents would be boosted for potent cancer therapy.

Methods

Materials. Unless otherwise noted, all the chemicals and reagents were obtained from commercial sources (J&K, TCI, Meryer or Sigma Aldrich). The solvents for reactions were distilled and degassed before use. All reactions were carried out in an N_2 atmosphere with a dried Schlenk glassware or tube. 4,9-Dibromo-6,7-diphenyl-[1,2,5]thiadiazolo[3,4-g]quinoxaline, tributyl(4-hexylthiophen-2-yl)stannane, 4,7-dibromobenzo[1,2-c:4,5-c']bis([1,2,5]thiadiazole) and *N,N*-diphenyl-4-(tributylstannyl)aniline were purchased from Nanjing Kaimuke Technology Co., Ltd. 1,2-Distearoyl-sn-glycero-3-phosphoethanolamine-N-[methoxy(polyethylene glycol)-2000 (DSPE-mPEG$_{2000}$) and FITC-labelled DSPE-PEG$_{2000}$ (DSPE-PEG$_{2000}$-FITC) were purchased from Xi'an Ruixi Biological Technology Co., Ltd. 2',7'-Dichlorodihydrofluorescein diacetate (DCFH-DA), fluorescein diacetate (FDA) and propidium iodide (PI) were purchased from Sigma-Aldrich. Apoptosis Assay Kit (Annexin V-APC/PI), Hoechst 33342 and Cell counting kit-8 (CCK-8) were purchased from Dojindo Laboratories. LysoTracker Red was purchased from Thermo Fisher. Roswell Park Memorial Institute-1640 medium, fetal bovine serum (FBS), and penicillin and streptomycin were purchased from Gibco.

Instrumentation. NMR spectra were obtained on Bruker AVIII 400 MHz NMR spectrometer. The [1]H

NMR (400 MHz) chemical shifts were recorded relative to CDCl$_3$ as the internal reference (CDCl$_3$: δ = 7.26 ppm). The ^{13}C NMR (100 MHz) spectra were given using CDCl$_3$ as the internal standard (CDCl$_3$: δ = 77.16 ppm). High-resolution mass spectra (HRMS) were obtained on a GCT premier CAB048 mass spectrometer operating in a MALDI-TOF mode. UV–Vis–NIR absorption spectra were measured on a PerkinElmer Lambda 950 spectrophotometer. Photoluminescence (PL) spectra were performed on an Edinburgh FLS1000 fluorescence Spectrofluorometer. Dynamic light scattering (DLS) for the analyses of particle size and storage stability was determined by Malvern Zetasizer Nano ZSP. The image from transmission electron microscopy (TEM) was obtained in a HITACHI-HT7700 transmission electron microscope. Photodynamic and photothermal therapy experiments were carried out by using an 808 nm infrared semiconductor laser (purchased from Changchun radium photoelectric technology). Photothermal images and temperature variations were recorded by an E6 camera with a FLIR System. CLSM images were observed on a confocal laser scanning microscope (LSM900, Carl Zeiss AG). The data of cell viability was determined by CCK-8 kit, and the absorbance of each sample was detected at 450 nm using a microplate reader (synergyH1, BioTek). The intravital fluorescence imaging was conducted on a commercial NIR-II in vivo imaging system (MARS-HS, Artemis Intelligent Imaging). Photoacoustic imaging experiments were performed using a commercial opto-acoustic imaging system (Vevo LAZR, Fuji Film Visual Sonics).

Cytotoxicity Evaluation. 4T1 cell (mouse breast cancer) line was purchased from Chinese Academy of Science Cell Bank for Type Culture Collection, and then grown in 1640 culture medium containing 10% FBS and 1% penicillin-streptomycin in a humidified environment of 5% CO$_2$ at 37 °C. 4T1 cells were seeded on 96-well plates at a density of 5×10^3 cells per well and incubated for one day. Then the growth medium was removed and replaced by a new culture medium containing 2TT-2BBTD NPs with different concentrations (0, 1, 2, 5, 10, 20 and 50 μM, determined by 2TT-2BBTD). After 12 h incubation, the cells were exposed to an 808 nm NIR laser (0.6 W/cm^2) and irradiated for 5 min. Meanwhile, the 2TT-2BBTD NPs incubated cells without light irradiation were also performed for the dark cytotoxicity evaluation. After further incubation (12 h), the media were removed and washed with PBS for three times. 4T1 cells were then incubated with fresh FBS-free medium containing CCK-8 (10%) for 2 h in the dark condition. Finally, the absorbance of the consequent products was recorded by a microplate reader at a wavelength of 450 nm. The results were expressed as the viable percentage of cells after various treatments relative to the control cells without any treatment. Hereof, the relative cell viability was determined according to the following formula: Cell viability (%) = (ODsample - ODbackground)/(ODcontrol - ODbackground) × 100%.

Animals and Tumor Model. All the relevant animal experiments involved in this study were approved by the Administrative Committee on Animal Research in Shenzhen Graduate School, Peking University (SYXK(YUE)2017-0172). Female BALB/c mice aged to 4~5 weeks were purchased from Beijing Vital River Laboratory Animal Technology. The mice were housed and fed with standard laboratory water and chow under pathogen-free conditions. The mentioned orthotopic 4T1 breast tumor model was successfully established through orthotopically injection of 4T1 cells (5×10^5) suspended in PBS buffer

into the upper right mammary fat pads. The 4T1 tumor-bearing mice were subsequently randomly used when the tumor volumes reached about 100 mm^3.

In Vivo Antitumor Efficacy. To evaluate the in vivo antitumor efficacy of 2TT-2BBTD NPs, the prepared orthotopic 4T1 breast tumor-bearing mice were randomly divided into four groups ($n = 5$), and named as "Saline", "Saline + L", "2TT-2BBTD NPs" and "2TT-2BBTD NPs + L". For "Saline" and "2TT-2BBTD NPs" groups, 200 µL of saline or 2TT-2BBTD NPs (2 mM determined by 2TT-2BBTD) were intravenously injected into the mice separately and without laser irradiation. In the cases of "Saline + L" and "2TT-2BBTD NPs + L", an 808 nm laser (0.6 W/cm^2) irradiation for 10 min was treated at the tumor site in each group after intravenously injection of saline or 2TT-2BBTD NPs (2 mM determined by 2TT-2BBTD) for 12 h, respectively. After various treatments, the mouse body weight as well as tumor volume were determined and recorded every 3 days during the 15-days study duration for counting the changes. The tumor size was measured by a vernier caliper, and then the tumor volume (V) was calculated using the formula: V = (length × $width^2$)/2. The relative tumor volume (RTV) was calculated as RTV = V/V_0, where V_0 was the initial tumor volume. The relative body weight (RBW) was calculated as RBW = $(W-W_0)/W_0$, where W_0 was the initial mouse body weight.

Data availability

All relevant data supporting the findings of this work are available from the corresponding authors upon reasonable request.

Acknowledgements

Author contributions

S.Y., Z.Z., D.W., and B.Z.T. conceived and designed the experiments. S.Y. performed the synthesis. S.Y., J.Z., and W.X. did the photophysical measurements and analyzed the data. J.Z. conducted theoretical calculations. Z.Z., M.K., and X.L. performed the biological experiments. D.Y., R.T.K.K., J.S., and J.W.Y.L. took part in the discussion and gave important suggestions. S.Y., J.Z., Z.Z., D.W., and B.Z.T. co-wrote the paper.

Competing interests

The authors declare no competing interests.

Reference

1. Regenmortel, M. H. V. Reductionism and complexity in molecular biology: scientists now have the tools to unravel biological complexity and overcome the limitations of reductionism. *EMBO Rep.* **5**, 1016–1020 (2004).

2. Pietronero, L. Complexity ideas from condensed matter and statistical physics. *Europhys. News.* **39**, 26–29 (2008).

3. Anderson, P. W. More is different: broken symmetry and the nature of the hierarchical structure of science. *Science.* **177**, 393–396 (1972).

4. Wood, J. The top ten advances in materials science. *Mater. Today.* **11**, 40–45 (2008).

5. Mei, J. et al. Aggregation-induced emission: the whole is more brilliant than the parts. *Adv. Mater.* **26**, 5429–5479 (2014).

6. Xu, Y. et al. Recent advances in luminescent materials for super-resolution imaging via stimulated emission depletion nanoscopy. *Chem. Soc. Rev.* **50**, 667–690 (2021).

7. Wong, M. Y. & Zysman-Colman, E. Purely organic thermally activated delayed fluorescence materials for organic light-emitting diodes. *Adv. Mater.* **29**,1605444 (2017).

8. Huang, J. & Pu, K. Near-infrared fluorescent molecular probes for imaging and diagnosis of nephro-urological diseases. *Chem. Sci.* **12**, 3379–3392 (2021).

9. Lei, Z. & Zhang, F. Molecular engineering of NIR-II fluorophores for improved biomedical detection. *Angew. Chem. Int. Ed.* **60**, 16294–16308 (2021).

10. Kang, M. et al. Aggregation-enhanced theranostics: AIE sparkles in biomedical field. *Aggregate.* **1**, 80–106 (2020).

11. Xu, S., Duan, Y. & Liu, B. Precise molecular design for high-performance luminogens with aggregation-induced emission. *Adv. Mater.* **32**, 1903530 (2020).

12. Förster, T. & Kasper, K. Ein konzentrationsumschlag der fluoreszenz. *Z. Phys. Chem.* (*Muenchen, Ger.*) **1**, 275–277 (1954).

13. Birks, J. B. Photophysics of aromatic molecules. Wiley: London, 1970.

14. Zhang, Z. et al. Semiconducting polymer dots with dual-enhanced NIR-IIa fluorescence for through-skull mouse-brain imaging. *Angew. Chem. Int. Ed.* **59**, 3691–3698 (2020).

15. Yang, S.-Y., Qu, Y.-K., Liao, L.-S., Jiang, Z.-Q. & Lee, S.-T. Research progress of intramolecular π-stacked small molecules for device applications. *Adv. Mater.* **34**, e2104125 (2022).

16. Mu, J. et al. The chemistry of organic contrast agents in the NIR-II window. *Angew. Chem. Int. Ed.* **61**, e202114722 (2022).

17. Yang, Q., Ma, H., Liang, Y. & Dai, H. Rational design of high brightness NIR-II organic dyes with S-D-A-D-S structure. *Acc. Mater. Res.* **2**, 170–183 (2021).

18. Xu, W., Wang, D. & Tang, B. Z. NIR-II AIEgens: a win-win integration towards bioapplications. *Angew. Chem. Int. Ed.* **60**, 7476–7487 (2021).

19. Cheng, P., Li, G., Zhan, X. & Yang, Y. Next-generation organic photovoltaics based on non-fullerene acceptors. *Nat. Photon.* **12**, 131–142 (2018).

20. Yan, C. et al. Non-fullerene acceptors for organic solar cells. *Nat. Rev. Mater.* **3**, 18003 (2018).

21. Wang, J. & Zhan, X. Fused-ring electron acceptors for photovoltaics and beyond. *Acc. Chem. Res.* **54**, 132–143 (2021).

22. Feng, K., Guo, H., Sun, H. & Guo, X. *n*-Type organic and polymeric semiconductors based on bithiophene imide derivatives. *Acc. Chem. Res.* **54**, 3804–3817 (2021).

23. Yang, G. et al. Acceptor engineering for optimized ROS generation facilitates reprogramming macrophages to M1 phenotype in photodynamic immunotherapy. *Angew. Chem. Int. Ed*. **60**, 5386–5393 (2021).

24. Ji, A. et al. Acceptor engineering for NIR-II dyes with high photochemical and biomedical performance. *Nat. Commun.* **13**, 3815 (2022).

25. Watson, W. F. & Livingston, R. Concentration quenching of fluorescence in chlorophyll solutions. *Nature.* **162**, 452–453 (1948).

26. Zhao, Z., Zhang, H., Lam, J. W. Y. & Tang, B. Z. Aggregation-induced emission: new vistas at the aggregate level. *Angew. Chem. Int. Ed*. **59**, 9888–9907 (2020).

27. Tu, Y., Zhao, Z., Lam, J. W. Y. & Tang, B. Z. Aggregate science: much to explore in the meso world. *Matter.* **4**, 338–349 (2021).

28. Zhang, Z. et al. An all-round athlete on the track of phototheranostics: subtly regulating the balance between radiative and nonradiative decays for multimodal imaging-guided synergistic therapy. *Adv. Mater.* **32**, 2003210 (2020).

29. Yang, J., Fang, M. & Li, Z. Organic luminescent materials: the concentration on aggregates from aggregation-induced emission. *Aggregate.* **1**, 6–18 (2020).

30. Qi, J., Ou, H., Liu, Q. & Ding, D. Gathering brings strength: how organic aggregates boost disease phototheranostics. *Aggregate*, **2**, 95–113 (2021).

31. Zhao, Z. et al. Highly efficient photothermal nanoagent achieved by harvesting energy via excited-state intramolecular motion within nanoparticles. *Nat. Commun*. **10**, 768 (2019).

32. Liu, S. et al. Constitutional isomerization enables bright NIR-II AIEgen for brain-inflammation imaging. *Adv. Funct. Mater.* **30**, 1908125 (2020).

33. Serrano-Andres, L., Merchan, M., Roos, B. O. & Lindh, R. Theoretical study of the internal charge transfer in aminobenzonitriles. *J. Am. Chem. Soc*. **117**, 3189–3204 (1995).

34. Grabowski, Z. R., Rotkiewicz, K. & Rettig, W. Structural changes accompanying intramolecular electron transfer: focus on twisted intramolecular charge-transfer states and structures. *Chem. Rev.* **103**, 3899–4032 (2003).

35. Zhang, Z. et al. The fast-growing field of photo-driven theranostics based on aggregation-induced emission. *Chem. Soc. Rev.* **51**, 1983–2030 (2022).

36. Qin, Y. et al. A self-assembled metallacage with second near-infrared aggregation-induced emission for enhanced multimodal theranostics. *J. Am. Chem. Soc.* **144**, 12825–12833 (2022).

37. Liu, S., Li, Y., Kwok, R. T. K., Lam, J. W. Y. & Tang, B. Z. Structural and process controls of AIEgens for NIR-II theranostics. *Chem. Sci.* **12**, 3427–3436 (2021).

38. Yan, D., Xie, W., Zhang, J., Wang, L. & Tang, B. Z. Donor/π-Bridge manipulation for constructing a stable NIR-II aggregation-induced emission luminogen with balanced phototheranostic performance.

Angew. Chem. Int. Ed. **60**, 26769–26776 (2021).

39. Shuai, Z. & Peng, Q. Organic light-emitting diodes: theoretical understanding of highly efficient materials and development of computational methodology. *Natl. Sci. Rev*. **4**, 224–239 (2017).

40. Peng, Q., Yi, Y. & Shuai, Z. Excited state radiationless decay process with duschinsky rotation effect: formalism and implementation. *J. Chem. Phys*. **126**, 114302 (2007).